

Structural investigation and photoluminescent properties of ZnWO₄:Dy³⁺ nanocrystals

R. F. Gonçalves¹ · E. Longo² · A. P. A. Marques¹ · M. D. P. Silva² · L. S. Cavalcante³ · I. C. Nogueira⁴ · I. M. Pinatti² · P. F. S. Pereira² · M. J. Godinho^{5,6}

Received: 26 April 2017 / Accepted: 29 June 2017 / Published online: 7 July 2017
© Springer Science+Business Media, LLC 2017

Abstract In this study, ZnWO₄:Dy³⁺ nanocrystals containing 0.5, 1, and 2 mol% of Dy³⁺ were synthesized by a coprecipitation method and grown in a microwave-assisted hydrothermal system at 140 °C for 1 h. X-ray diffraction, Rietveld refinement, and Fourier transform Raman and infrared spectroscopy analyses indicated that each of the crystals had a wolframite-type monoclinic structure, with no other phases present. Structural refinement was carried out to model the distorted octahedral [ZnO₆], [DyO₆], and [WO₆] clusters. Furthermore, transmission scanning electron microscopy images revealed interesting crystal morphologies and a decrease of the average crystal size, which were dependent on the Dy³⁺ doping concentration. Ultraviolet–Visible diffuse reflectance spectra indicated that the optical band gap increases with increasing replacement of Zn²⁺ by Dy³⁺ ions. The photoluminescent properties,

chromaticity coordinates, and lifetimes of the ZnWO₄:Dy³⁺ nanocrystals were studied.

1 Introduction

Zinc tungstate (ZnWO₄) is a divalent transition-metal tungstate with the general formula AWO₄. ZnWO₄ crystallizes in a monoclinic wolframite structure [1, 2], and is a promising material that has received considerable attention for applications in luminescent devices, solid-state laser hosts, optical and acoustic fibers, humidity and gas sensors, and scintillation materials [3, 4]. The broad range of applications of ZnWO₄ arises from its excellent chemical stability and optical properties, such as high average refractive index, high X-ray absorption coefficient, high light yield, short decay time, long afterglow luminescence, and dielectric and magnetic properties [5, 6]. Furthermore, several nanocrystalline zinc tungstates doped with different rare earth metals have been shown to have suitable optical properties for applications in photonics owing to their enhanced luminescence properties [7, 8]. These materials are a possible alternative to existing lighting technologies, especially from the viewpoint of energy savings and reduced operating costs [9].

In light of these potential applications, many methodologies have been developed to synthesize, characterize, and study the properties of nanoscale metal tungstates, including solvothermal [10], Czochralski [11], sonochemical [12] and conventional hydrothermal [13] methods. Among the various synthetic techniques, the microwave-assisted hydrothermal (MAH) method has proven to be an efficient and convenient approach to fabricate inorganic materials with controlled particle sizes and morphologies, which are

Electronic supplementary material The online version of this article (doi:10.1007/s10854-017-7434-0) contains supplementary material, which is available to authorized users.

✉ R. F. Gonçalves
rosanaf.gon@gmail.com

¹ UNIFESP-Universidade Federal de São Paulo, Rua Prof. Artur Riedel, 275, Diadema, SP 09972-270, Brazil

² CDMF-DQ, Universidade Federal de São Carlos, P.O. Box 676, São Carlos, SP 13565-905, Brazil

³ PPGQ, Universidade Estadual do Piauí, Rua João Cabral, 2231, P.O. Box 381, Teresina, PI 64002-150, Brazil

⁴ IFMA-Instituto Federal do Maranhão, Avenida Getúlio Vargas, Monte Castelo, São Luís, MA 65030-005, Brazil

⁵ DEMA, Universidade Federal de São Carlos, São Carlos, SP 13565-905, Brazil

⁶ Departamento de Química-CAC, UFG-Universidade Federal de Goiás, Catalão, GO 75704-020, Brazil

properties that must be controlled to ensure superior physical properties [14].

Microwave heating is a fast, simple, and efficient method to prepare nanosized inorganic materials [15, 16]. Owing to its alternating electromagnetic fields, microwave irradiation induces rotation of polar molecules (those with a dipole moment) or ionic aggregates, causing molecular-level heating, and leading to homogeneous and rapid thermal reactions with low thermal gradients [17].

One of the most promising applications of metal tungstates is as single sources of white light. As the tungstate matrix itself has blue-green emission, combining metal tungstates with the characteristic narrow-line emission of doped lanthanide ions can yield white light [18, 19].

Generally, blue, green, and red emitting phosphors with the correct emission proportions are necessary to achieve white light emission. Consequently, at least two different phosphor matrices doped with different rare earth materials are required, which may be costly. However, in the case of some Dy³⁺-doped phosphors, only a single dopant and single host are required for the generation of white light, effectively reducing the cost of the material [20]. Dy³⁺ ions are useful because of their potential applications in optical devices and lasers when used as dopants in a variety of materials [21]. In addition, several other phosphor hosts doped with Dy³⁺ that emit white or near white light have been studied.

The photoluminescence (PL) emission spectra of different phosphors contain at least two peaks; for example, Sr₂SiO₄ [22], Sr₃Y(PO₄)₃ [23], Sr₂MgAl₂O₆ [24], Sr₂MgSi₂O₇ [25], and YAlO₃ [26] doped with Dy³⁺ ions emit near-white light due to adjustment of the yellow to blue intensity ratio. In general, Dy³⁺ ions provide two dominant emission bands that originate from ⁴F_{9/2} → ⁶H_{15/2} (blue) and ⁴F_{9/2} → ⁶H_{13/2} (yellow) transitions [27, 28]. Kuang et al. [29] studied the photoluminescent properties of Dy³⁺-doped SrSiO₃ phosphors, and they observed that these phosphors emit white light after irradiation for 5 min with 254 nm UV light. However, despite considerable research into rare-earth-doped phosphor matrices, there is a lack of detailed luminescence data beyond the recorded emission and excitation spectra for new hosts, new dopants, and new light emission wavelengths.

In previous publications [30, 31], the synthesis and characterization of efficient luminescent zinc tungstate nanostructures, both pure and doped with Er³⁺ or Sm³⁺, have been described, and these materials were found to be very promising candidates for electronic and optical applications. Thus, studies of the effect of different rare earth dopants on the synthesis and optical properties of zinc tungstate nanostructures are required to understand and improve their photoluminescent properties and applications.

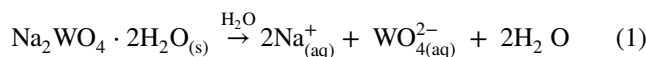
To the best of our knowledge, few studies concerning Dy³⁺-doped ZnWO₄ have been published. Dabre and Dhoble [32] reported the photoluminescence of Dy³⁺-activated ZnWO₄ synthesized via a solid state route at 850 °C. In another study [27], Eu³⁺/Dy³⁺ co-doped ZnWO₄ phosphors were synthesized via a hydrothermal method followed by calcination. However, these studies either employed higher synthesis temperatures than those used herein, resulting in larger particle sizes (about 2–3 μm), or used a combination of two rare earth ions to achieve white-light emission, which is disadvantageous. Furthermore, no investigation of the structural properties involving refinement of the structural data was presented. Data obtained by Rietveld refinement, as presented herein, are extremely useful for elucidating the details of the structure and electronic properties of these materials. On the other hand, Phuruangrat et al. [33] reported the photocatalytic properties of Dy-doped ZnWO₄ nanorods synthesized by the hydrothermal method, but they did not study the photoluminescence properties.

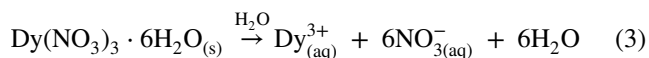
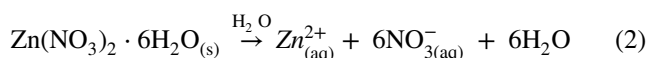
Therefore, in this paper, we demonstrate novel structural and PL properties of nanostructured ZnWO₄ doped with Dy³⁺ at different dopant ion concentrations. We report, for the first time, the structural and electronic details of this system.

2 Experimental details

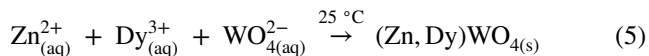
2.1 Synthesis and microwave-assisted hydrothermal processing of ZnWO₄:Dy³⁺ nanocrystals

ZnWO₄:Dy³⁺ crystals containing 0.5, 1, and 2 mol% Dy³⁺ were synthesized by the coprecipitation (CP) method at room temperature using sodium tungstate(VI) dihydrate [Na₂WO₄·2H₂O] (99% purity, Sigma–Aldrich), zinc nitrate hexahydrate [Zn(NO₃)₂·6H₂O] (99.5% purity, Aldrich), and dysprosium(III) nitrate hexahydrate [Dy(NO₃)₃·6H₂O] (99.999% purity, Aldrich). First, 5 × 10^{−3} mol of Na₂WO₄·2H₂O was dissolved in deionized water (50 mL) with constant stirring. Separately, 5 × 10^{−3} mol of [Zn(NO₃)₂·6H₂O] was dissolved in deionized water (50 mL) with constant stirring at pH 6, and an appropriate amount (0.5, 1, and 2 mol%) of Dy(NO₃)₃ was added to the aqueous solutions containing Zn²⁺ ions. The Zn²⁺ solution was added to the WO₄^{2−} solution and heated at 90 °C with constant stirring for 30 min. Instantaneously, a white suspension formed. These Dy³⁺/Zn²⁺ solutions were then sealed in a Teflon autoclave. The reactions of Dy³⁺/Zn²⁺ and WO₄^{2−} resulted in the formation of crystalline ZnWO₄:Dy³⁺ precipitates, as described by Eqs. (1–5):





After CP at room temperature:



Finally, to carry out the MAH synthesis, the Teflon autoclave was placed inside a microwave system (2.45 GHz, with a maximum power of 800 W), and the solutions were processed at 140 °C for 1 h. The heating rate in this system was fixed at 25 °C min⁻¹, and the pressure inside the autoclave was stabilized at 245 kPa. After processing, the autoclave was allowed to cool slowly to room temperature. The resulting suspension was washed with deionized water several times to neutralize the solution (pH7). The white precipitates were collected and dried at 60 °C. Finally, the powders were heat treated at 700 °C for 30 min in a microwave furnace.

2.2 Characterization of ZnWO₄:Dy³⁺ nanocrystals

The ZnWO₄:Dy³⁺ nanocrystals were structurally characterized by X-ray diffraction (XRD) using a D/Max-2500PC diffractometer (Rigaku, Japan), with Cu-K α radiation ($\lambda=1.5406 \text{ \AA}$) in the 2θ range from 10° to 110° at a scanning rate of 0.02° min⁻¹; the total collection time was 20 min. Rietveld refinement was performed on the data collected in the 2θ range of 10°–110° with a scanning rate of 0.02° min⁻¹ (collection time of 110 min). The Fourier transform (FT)-Raman spectra were recorded between 50 and 1050 cm⁻¹ using an RFS100 spectrophotometer (Bruker, Germany) equipped with a Nd:YAG laser ($\lambda=1,064 \text{ nm}$). The laser power on the sample was fixed at 100 mW and counts were collected over 500 scans. The FT-infrared (IR) spectra were recorded between 200 and 1,000 cm⁻¹ with an MB-102 spectrophotometer (Bomem-Michelson, Switzerland) in transmission mode. The crystal shapes and sizes were observed using high-resolution transmission electron microscopy (HR-TEM) using a Tecnai G2-F20 microscope (200 kV). Ultraviolet–Visible (UV–Vis) spectra were recorded using a Varian spectrophotometer (Cary 5 G, USA) in diffuse reflectance mode. The luminescence study was based on the excitation and emission spectra recorded at room temperature (300 K). The data were obtained by using a 1940D spectrofluorometer (HORIBA,

Jobin Yvon–Fluorolog III) with double monochromators in front face mode (22.5°) with a USHIO™ UXL-450SO 450 W xenon gas discharge lamp as the excitation source. For acquisition of the emission spectra ($\lambda_{\text{ex}}=298 \text{ nm}$; range: 400–700 nm), the excitation and emission slits were both set to 1.00 nm. For acquisition of the excitation spectra ($\lambda_{\text{em}}=580 \text{ nm}$; range: 270–460 nm), the excitation and emission slits were both set to 0.50 nm. The excitation spectra were corrected by using a reference detector. In both cases, the increment was 1.00 nm and the integration time was 0.5 s. Luminescence decay curves were recorded with a SPEX1934D phosphorimeter accessory with an EXCELITAS™ FX-1102 Short Arc Xenon Flashlamp (0.15 J per flash, 10 W average power, 300 Hz flash rate. Time per flash: 60 ms, delay increment: 0.05 ms). X-ray Photoelectron Spectroscopy (XPS) was performed using a ScientaOmicron ESCA + spectrometer with a high-performance hemispheric analyzer (EA 125) with monochromatic Al K α ($h=1486.6 \text{ eV}$) radiation as the excitation source. The operating pressure in the ultrahigh vacuum chamber (UHV) during analysis was 2×10^{-9} mbar. Energy steps of 50 and 20 eV were used for the survey and high resolution spectra, respectively.

3 Results and discussion

3.1 XRD pattern analyses

Figure 1a–c show the XRD patterns of ZnWO₄:Dy³⁺ nanocrystals containing 0.5, 1, and 2 mol% Dy³⁺

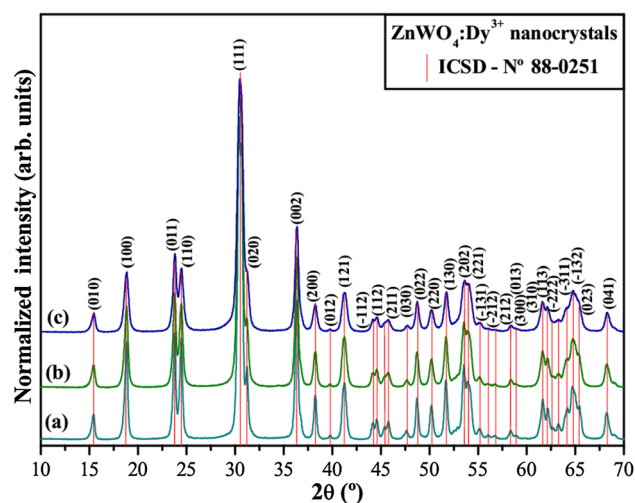


Fig. 1 XRD patterns of the ZnWO₄:Dy³⁺ nanocrystals with various amounts of Dy³⁺: (a) 0.5, (b) 1, and (c) 2 mol%. The vertical lines indicate the relative positions of diffraction peaks described in ICSD N° 88–0251

synthesized by the CP method and processed in the MAH system at 140 °C for 1 h. The XRD patterns were used to evaluate the long-range structural order–disorder and lattice periodicity. All diffraction peaks observed in the diffractograms in Fig. 1(a–c) could be indexed to a wolframite-type structure in the monoclinic space group $P2/c$ (Inorganic Crystal Structure Database (ICSD) No. 88–0251). No other phases were observed in the diffractograms. The presence of strong and sharp diffraction peaks, as shown in Fig. 1a–c, is a typical characteristic of well-ordered, crystalline materials. The Dy^{3+} dopant concentration was very low; therefore, no shift of the XRD peaks was observed.

3.2 Rietveld refinement analyses

The measured XRD patterns were subjected to Rietveld refinement, carried out using the general structure

analysis (GSAS) program [34]. The Rietveld method is based on the construction of theoretical diffraction patterns calculated according to a structural model [35]. The fit of the calculated pattern to the observed data and subsequent refinement provide the structural parameters of the material and the diffraction profile. The background was corrected using a first-order Chebyshev polynomial. The diffraction peak profiles were adjusted using a Thompson–Cox–Hastings pseudo-Voigt (pV–TCH) [36] function by employing the asymmetry function described by Finger et al. [37], which allowed us to account for asymmetry due to axial divergence. To account for anisotropy in the half-width of the reflections, the Stephens [38] model was used. In this work, the Rietveld refinement was carried out to investigate the substitution of Zn^{2+} ions by Dy^{3+} ions in the crystalline structure ZnWO_4 .

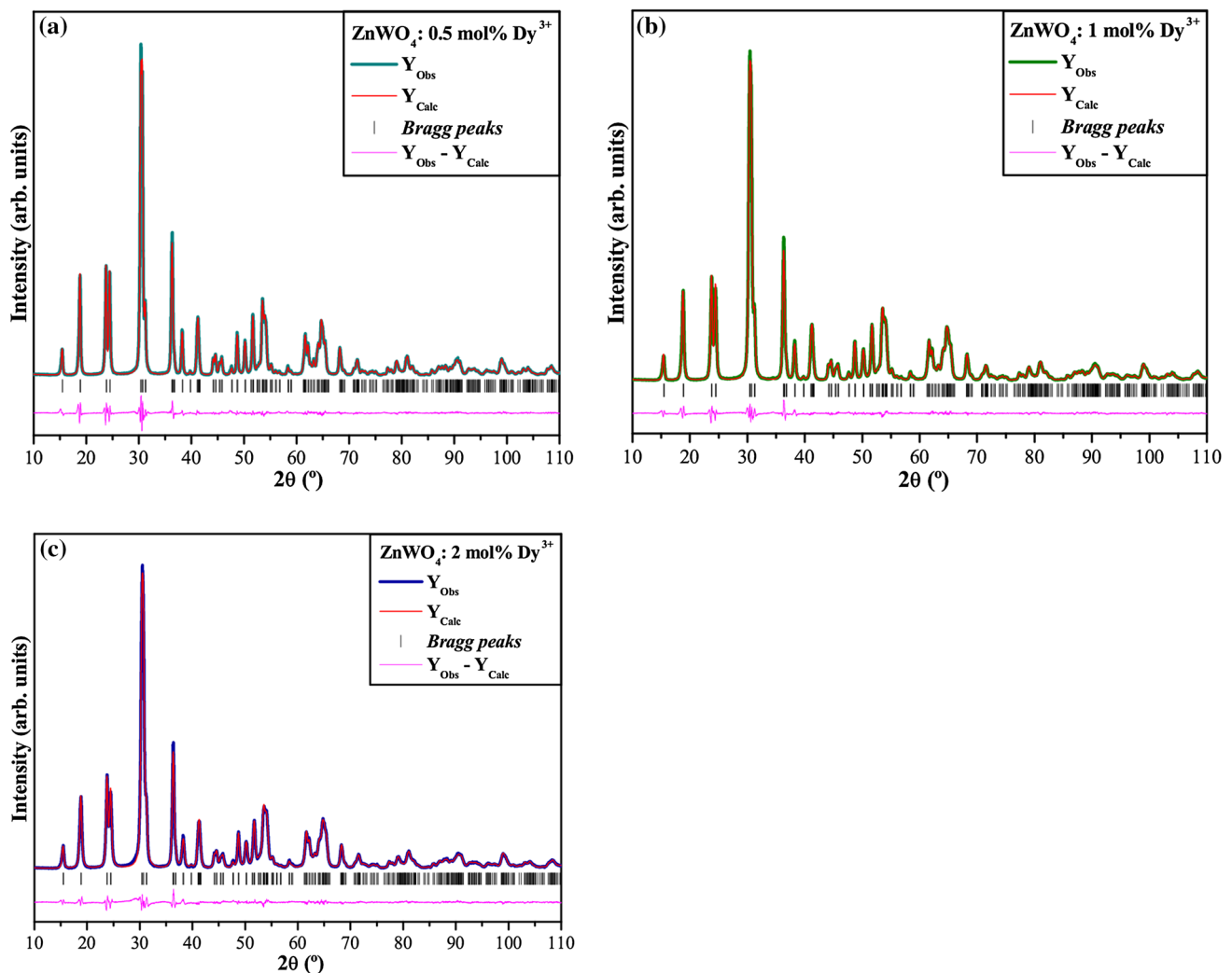


Fig. 2 Rietveld refinements plot of the $\text{ZnWO}_4:\text{Dy}^{3+}$ nanocrystals containing Dy^{3+} ions at: **a** 0.5, **b** 1, and **c** 2 mol%, respectively

Figure 2a–c show the Rietveld refinement plots for the observed patterns versus the calculated patterns of $\text{ZnWO}_4\text{:Dy}^{3+}$ nanocrystals.

The measured diffraction patterns are well matched to ICSD card No. 88–0251 [39], confirming that the $\text{ZnWO}_4\text{:Dy}^{3+}$ crystals crystallize in the monoclinic space group $P2/c$ with two formula units per unit cell ($Z=2$). The crystals contain a single phase, i.e., some Zn^{2+} ions were replaced by Dy^{3+} ions while maintaining the ZnWO_4 crystal structure, confirming the efficacy of our synthetic method. The obtained data listed in Table 1 show the small deviations of the statistical parameters, such as the weighted profile R-factor (R_{wp}), Bragg R-factor (R_{Bragg}), profile R-factor (R_{p}), and goodness of fit (χ^2 or “Chi squared”); the statistical results are indicative of the high quality of the structural refinement and numerical results. Table 1 also contains the lattice parameters and unit cell volume of each sample. The numbers in parentheses are the errors of the lattice parameters and cell volume, calculated by using the general structure analysis (GSAS) program. The structure obtained by Rietveld refinement is in good agreement with the observed XRD patterns and theoretical result.

3.3 Unit cell of $\text{ZnWO}_4\text{:Dy}^{3+}$ crystals

The lattice parameters and atomic positions obtained by Rietveld refinement and listed in Table 1 were used to model the monoclinic $(\text{Zn, Dy})\text{WO}_4$ structure (Fig. 3).

These unit cells were modeled using the VESTA program [40] (version 3 for Windows®). In Fig. 3, the O–W–O and O–Zn–O bonds are shown. In these unit cells, tungsten atoms are coordinated with six oxygen atoms to form octahedral $[\text{WO}_6]$ clusters. These octahedral $[\text{WO}_6]$ clusters are slightly distorted in the lattice of the $\text{ZnWO}_4\text{:Dy}^{3+}$ nanocrystals and the differences in the O–W–O bond angles lead to different levels of order–disorder and/or distortions in the $\text{ZnWO}_4\text{:Dy}^{3+}$ crystal lattice (Fig. 3). In addition, zinc atoms are bonded to six oxygen atoms, resulting in the formation of octahedral $[\text{ZnO}_6]$ clusters with $P2/c$ symmetry. Thus, the $[\text{DyO}_6]$ clusters have the same electronic coordination as the $[\text{ZnO}_6]$ clusters in the A-site.

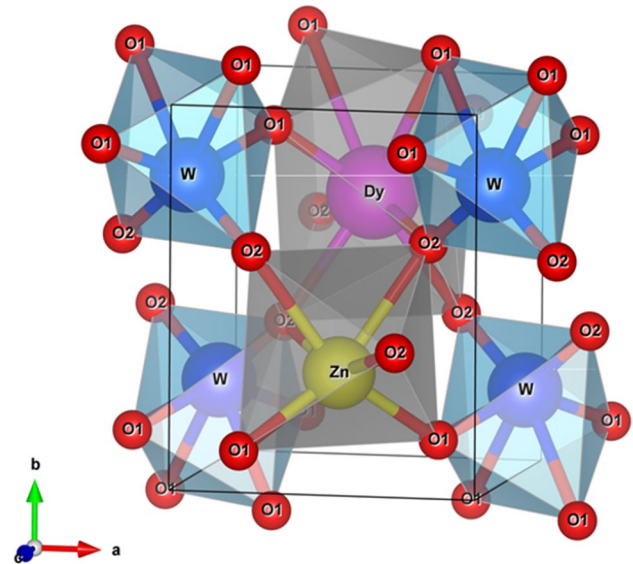


Fig. 3 Unit cell representation for $\text{ZnWO}_4\text{:Dy}^{3+}$ nanocrystals

3.4 FT-Raman and FT-IR spectral analyses

Raman spectroscopy is a powerful tool for analyzing the structures of ceramic materials. Using this technique, the presence of structural defects, as well as the short-range organization of the ceramic framework, can be determined. Raman spectroscopy is based on the inelastic scattering of photons, which lose energy by exciting vibrations in the sample. Figure 4 shows the MR spectra of the synthesized ZnWO_4 samples.

Based on group theory calculations and the symmetries of tungstates and molybdates with wolframite-type monoclinic structures, these structures have $3N=36$ degrees of freedom for $N=12$ atoms present inside the unit cell (monoclinic). Thus, the Raman and IR spectra will exhibit 36 different vibrational modes, which are represented by Eq. (6):

$$\Gamma_{(\text{Raman} + \text{Infrared})} = 8A_g + 10B_g + 8A_u + 10B_u \quad (6)$$

where A_g and B_g are active vibrational modes in the Raman spectrum, and A_u and B_u are active vibrational modes in the

Table 1 Lattice parameters, unit cell volume, and statistical parameters of quality obtained by Rietveld refinement of the $\text{ZnWO}_4\text{:Dy}^{3+}$ nanocrystals

[Dy ³⁺]/(mol%)	Lattice parameters					Cell volume (Å ³)
	a (Å)	b (Å)	c (Å)	$\alpha=\gamma$ (°)	β (°)	
0.5 ^a	4.70016 (9)	5.72087 (10)	4.93113 (8)	90°	90.7274 (15)	132.5830 (30)
1 ^b	4.70209 (10)	5.72063 (10)	4.93277 (9)	90°	90.7294 (16)	132.675 (4)
2 ^c	4.70393 (15)	5.71921 (15)	4.93458 (13)	90°	90.7446 (24)	132.743 (5)
ICSD-88-0251	4.69263 (5)	5.72129 (7)	4.92805 (5)	90°	90.6320 (9)	132.3

^a R_{Bragg} (%) = 2.22; χ^2 (%) = 1.95; R_{wp} (%) = 7.85; R_{p} (%) = 5.54

^b R_{Bragg} (%) = 1.77; χ^2 (%) = 1.70; R_{wp} (%) = 6.90; R_{p} (%) = 4.89

^c R_{Bragg} (%) = 2.03; χ^2 (%) = 1.84; R_{wp} (%) = 7.65; R_{p} (%) = 5.22

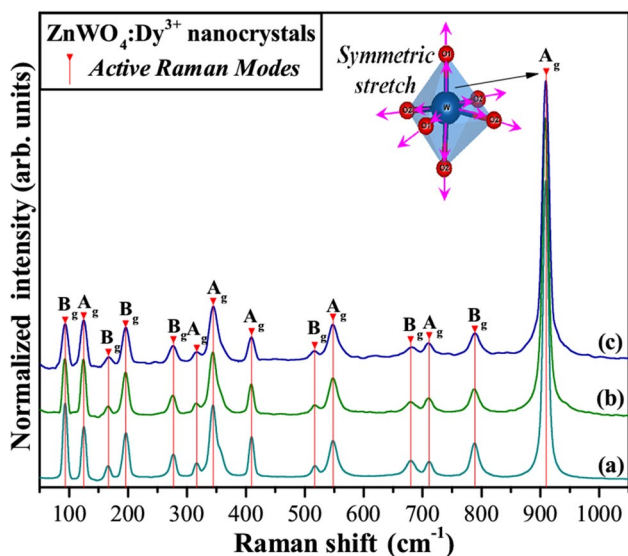


Fig. 4 FT-Raman spectra of the ZnWO₄:Dy³⁺ nanocrystals containing Dy³⁺ ions at: (a) 0.5, (b) 1, and (c) 2 mol%

IR spectrum. Therefore, only 18 active vibrational modes are expected in the Raman spectrum of ZnWO₄ crystals, as represented by Eq. (7):

$$\Gamma_{\text{(Raman)}} = 8A_g + 10B_g \tag{7}$$

The Raman spectra of tungstates can be classified into two modes: external and internal [41]. The external vibrational modes are related to network phonons, which correspond to the movement of distorted octahedral [ZnO₆] clusters in the unit cell. The internal vibrational modes are related to the vibrations of distorted octahedral [WO₆] clusters, assuming a steady-state center of mass.

The vibrational Raman active modes between 50 and 1100 cm⁻¹ of ZnWO₄:Dy³⁺ nanocrystals are shown in the FT-Raman spectra (Fig. 4a–c).

The presence of well-defined Raman peaks indicates that the crystals have good short-range structural order. All Raman-active modes in the ZnWO₄ nanocrystals observed in Fig. 4a–c were identified and designated as either A_g or B_g. The most intense Raman bands observed at 905 and 344 cm⁻¹ correspond to stretching vibrations of W–O bonds in the WO₆ octahedra. The bands at 783, 544, 406, 192, and 123 cm⁻¹ originate from symmetric stretching of the ZnO₆ octahedra, and the others bands in the 400–600 cm⁻¹ region can be assigned to modes associated with Zn–O stretching. The bands located 707 and 675 cm⁻¹ correspond to the motions of the WO₆ octahedra against Zn²⁺, while the bands in the 500–600 cm⁻¹ range are characteristic of symmetric W–O–W stretching modes [42].

There is excellent agreement between the positions of the Raman modes for ZnWO₄ nanocrystals obtained in this work and those reported previously for samples prepared by other methods [43]. However, when comparing the positions of the Raman peaks, there are some minor variations that may be related to factors such as the average size of the nanocrystals, variation in the bond length, interactions between the [ZnO₆] and [WO₆] clusters, and different degrees of distortion of the octahedral [ZnO₆] and [WO₆] clusters in the crystal lattice. Such differences result from experimental variables such as temperature, time, and methodology.

FT-IR spectroscopy was used to evaluate the degree of structural order–disorder in the metal–oxygen bonds, which is determined by the symmetry of the molecule and the functional groups present. While Raman spectroscopy selection rules require that the molecular polarizability changes during the vibration, IR spectroscopy requires that, upon the absorption of a photon, the dipole moment of the molecule changes during the vibration.

As described above, the Raman and IR spectra exhibit 36 different vibrational modes. Among these modes, only some are IR active. Therefore, only 18 vibrational modes are expected in the IR spectrum of the ZnWO₄ crystals, as represented by Eq. (8):

$$\Gamma_{\text{(Infrared)}} = 8A_u + 10B_u \tag{8}$$

However, three of these modes (1A_u and 2B_u) are acoustic vibrations and, therefore, cannot be detected in the IR spectrum. Thus, Eq. (8) must be reduced and is better represented by Eq. (9):

$$\Gamma_{\text{(Infrared)}} = 7A_u + 8B_u \tag{9}$$

In general, IR spectroscopy measures the vibration modes between atoms that are bonded together. In this work, IR transmission measurements were used to monitor the metal–oxygen bonds that vibrate in the low wave-number region. The stretching absorption bands (symmetric, asymmetric, and anti-symmetric) for the bonds between the metal ions and oxygen can be observed.

In the FT-IR spectrum of the ZnWO₄:Dy³⁺ nanocrystals illustrated in Fig. 5a–c, seven active vibrational modes between 400 and 1000 cm⁻¹ can be identified. This is the mid-IR region, where molecular vibrations can be detected. The bands at 473 and 611 cm⁻¹ are assigned to bending vibrations of the W–O bonds. The peaks at 701 and 838 cm⁻¹ correspond to stretching vibration of the W–O bonds. The Zn–O–W bond vibrations result in a strong peak at 880 cm⁻¹ owing to bending and stretching deformations. For the ZnO₆ and WO₆ octahedra, the symmetric and asymmetric deformation modes of the W–O and Zn–O bonds are observed at 534 and 432 cm⁻¹, respectively [44].

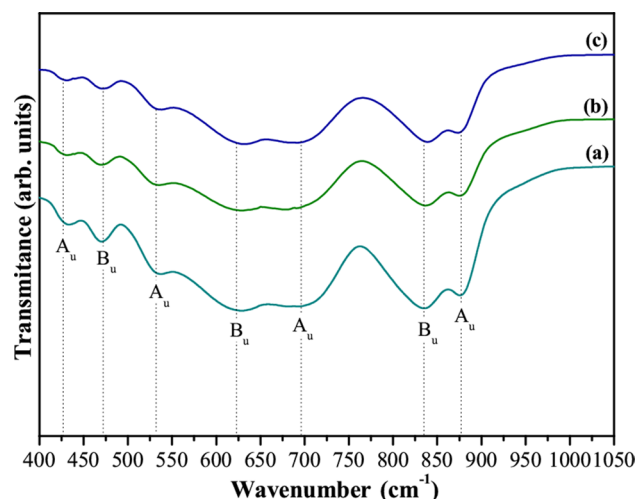


Fig. 5 FT-IR spectra of the $\text{ZnWO}_4\text{:Dy}^{3+}$ nanocrystals containing Dy^{3+} ions at: (a) 0.5, (b) 1, and (c) 2 mol%

3.5 HR-TEM image analyses

Figure 6a–i show TEM images of the $\text{ZnWO}_4\text{:Dy}^{3+}$ nanocrystals containing 0.5, 1, and 2 mol% Dy^{3+} synthesized by the CP method and processed in the MAH system at 140 °C for 1 h.

TEM was used to evaluate the particle size, homogeneity, and shape of the crystals. In the field of optoelectronics, the morphology of materials has a significant effect on their application to nanodevices. Structures such as rods, spheres, tubes, and tapes are examples of morphologies that have unique properties for this purpose [45]. Figure 6a–i show the spherical-like $\text{ZnWO}_4\text{:Dy}^{3+}$ nanocrystals. The obtained nanospheres were formed without any kind of template, capping agents, surfactant, or catalyst, and solely occur as a result of the methodology used. The image shows uniform size distribution and agglomerated sheets of nanoparticles. Consequently, we believe that increasing the Dy^{3+} ion content in the compounds promotes a change in the crystal growth, potentially reducing the size of the crystals. TEM images were crucial to evaluating the average crystal size distribution by counting 300 crystals for a good surface contour to ensure the authenticity of the statistical response (Figs. S1a–c See Supplementary Information). The particle size decreased with increased Dy^{3+} doping. The particles in the sample with 2 mol% of Dy^{3+} had an average size of approximately 21.26 nm, whereas the average particle sizes for the samples doped with 0.5 and 1 mol% Dy^{3+} were 36.01 and 30.77 nm, respectively. In addition, the particle shapes affect the optical properties, and the obtained nanospheres have excellent photoluminescent properties (Fig. 9a–c). These properties are strongly

dependent on the surface area, crystallinity, and orientation of the nanoparticles.

Recently, developments in the understanding of the structure–property relationships of nanocrystals have shown that the material properties are highly dependent on the crystal size and, in particular, on size-induced modifications to the band structure [33, 46].

3.6 UV–Vis diffuse reflectance spectroscopy analyses

Optical band gap energy (E_{gap}) values were calculated using the Kubelka–Munk equation [48], which is based on the transformation of diffuse reflectance measurements to accurately estimate E_{gap} values. In particular, the Kubelka–Munk equation is useful in the case of infinitely thick samples. The Kubelka–Munk equation at any wavelength is given by:

$$\frac{K}{S} = \frac{(1 - R_{\infty})^2}{2R_{\infty}} \equiv F(R_{\infty}) \quad (10)$$

where $F(R_{\infty})$ is the Kubelka–Munk function, that is, the absolute reflectance of the sample. In our case, magnesium oxide (MgO) was used as the standard sample in reflectance measurements, so $R_{\infty} = R_{\text{sample}}/R_{\text{MgO}}$ (R_{∞} is the reflectance), K is the molar absorption coefficient, and S is the scattering coefficient. In a parabolic band structure, the optical band gap and absorption coefficient of semiconductor oxides can be calculated using Eq. (11):

$$\alpha h\nu = C_1(h\nu - E_{\text{gap}})^n \quad (11)$$

where, α is the linear absorption coefficient of the material, $h\nu$ is the photon energy, C_1 is a proportionality constant, E_{gap} is the optical band gap, and n is a constant associated with different kinds of electronic transitions ($n=1/2$ for a direct allowed, $n=2$ for an indirect allowed, $n=1.5$ for a direct forbidden, and $n=3$ for an indirect forbidden transition). According to theoretical calculations reported in the literature [48], the optical absorption spectrum of ZnWO_4 nanocrystals is governed by direct electronic transitions. Consequently, after the electronic absorption process, electrons located in minimum energy states in the conduction band (CB) are able to return to maximum energy states of the valence band (VB), which are at the same points in the Brillouin zone [49]. Based on this information, the E_{gap} values of $\text{ZnWO}_4\text{:Dy}^{3+}$ nanocrystals were calculated using $n=1/2$ in Eq. (11). Finally, using the diffuse reflectance function described in Eq. (10) with $K=2\alpha$, we obtain the modified Kubelka–Munk equation, as shown in Eq. (12):

$$[F(R_{\infty})h\nu]^2 = C_2(h\nu - E_{\text{gap}}) \quad (12)$$

Therefore, the $F(R_{\infty})$ values were found using Eq. (12) and a graph of $[F(R_{\infty})h\nu]^2$ against $h\nu$ was plotted to

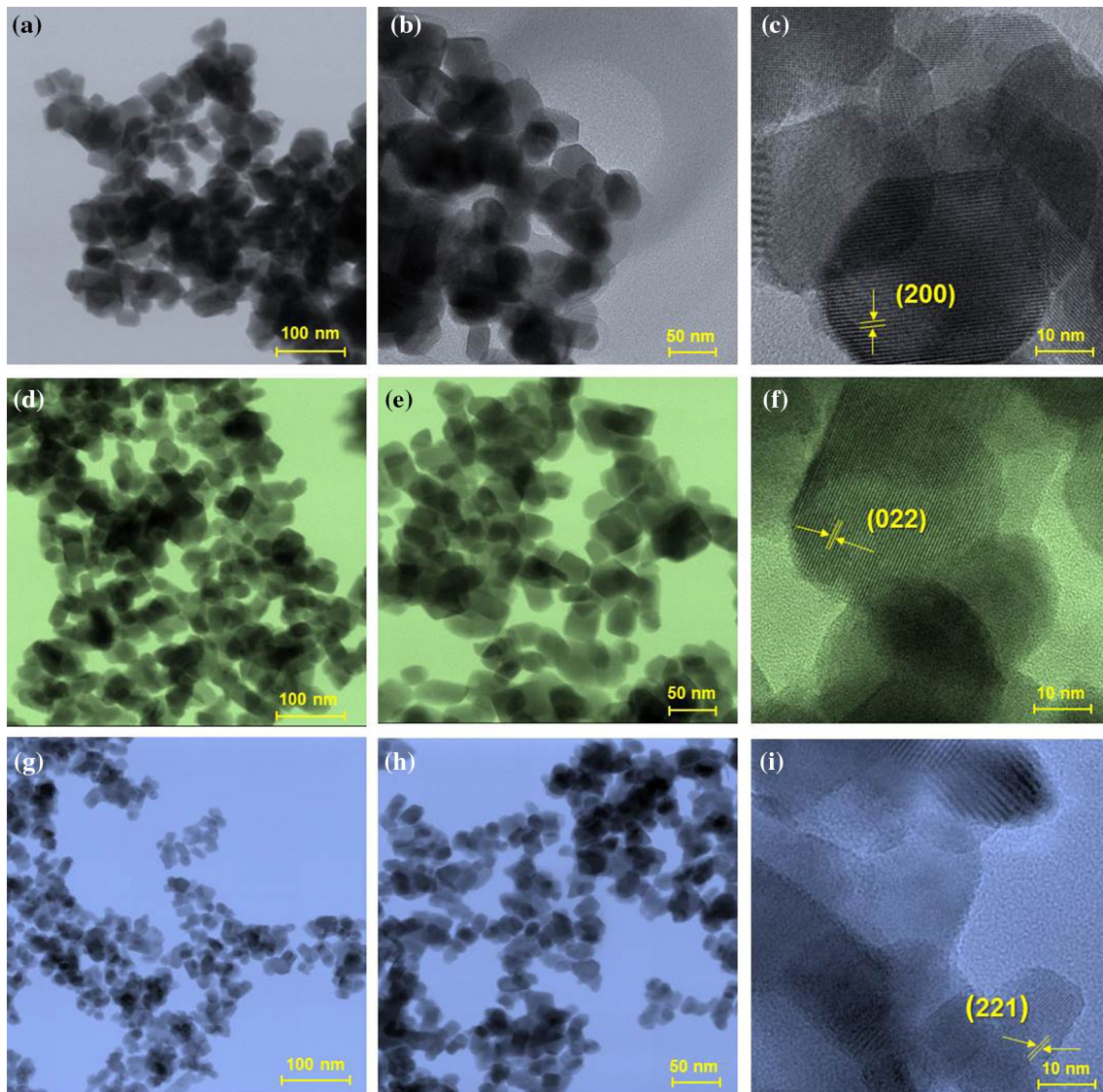


Fig. 6 HR-TEM images of the $\text{ZnWO}_4:\text{Dy}^{3+}$ nanocrystals with various amounts of Dy^{3+} : **a, b, c** 0.5, **d, e, f** 1, and **g, h, i** 2 mol%

calculate the E_{gap} values for $\text{ZnWO}_4:\text{Dy}^{3+}$ nanocrystals by extrapolating the linear portion of the UV–vis curves.

Figure 7a–c show the UV–Vis spectra of the $\text{ZnWO}_4:\text{Dy}^{3+}$ nanocrystals obtained by CP at room temperature and processed at 140°C for 1 h in the MAH system. The band gaps are estimated to be 3.18, 3.19, and 3.22 eV for the ZnWO_4 crystals with 0.5, 1, and 2 mol% of Dy^{3+} , respectively.

Figure 7a–c reveal that the E_{gap} values tend to increase with increasing Dy^{3+} ion concentration. This behavior is likely related to the presence of intermediary energy levels between the VB and CB and electronic energy levels related to the additional $4f$ orbitals of the Dy^{3+} ions present in the lattice nanocrystals. This effect serves as further evidence for the incorporation of Dy^{3+} into the ZnWO_4 host

matrix. With an increase in the Dy^{3+} concentration, the characteristics of the $\text{ZnWO}_4:\text{Dy}^{3+}$ crystals tend toward those of dysprosium oxide (Dy_2O_3). Dy_2O_3 has a band gap of 4.9 eV [50, 51], and the band gap energies of the synthesized compounds increase as the Dy^{3+} concentration in the structure increases. In addition to doping, we believe that the E_{gap} values are also related to factors such as morphology, particle shape, and size.

3.7 Photoluminescence

The PL excitation spectra of ZnWO_4 doped with 0.5, 1, and 2 mol% of Dy^{3+} , recorded by monitoring the ${}^4\text{F}_{9/2} \rightarrow {}^6\text{H}_{13/2}$ transition at 580 nm, are shown in Fig. 8. The excitation spectra contain a strong band with a maximum at 298 nm,

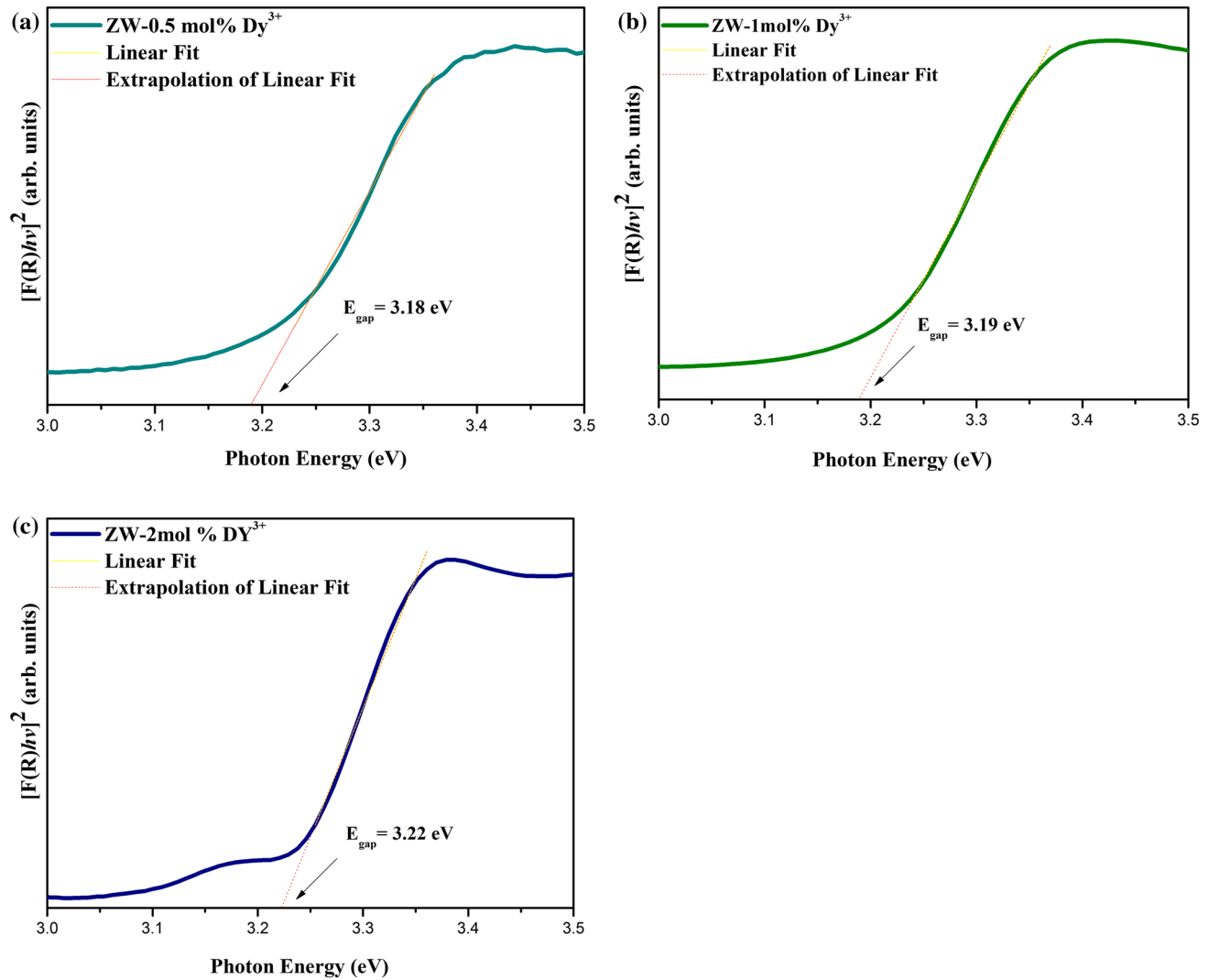


Fig. 7 UV-Vis spectra of the $\text{ZnWO}_4:\text{Dy}^{3+}$ nanocrystals containing **a** 0.5, **b** 1, and **c** 2 mol% of Dy^{3+} ions

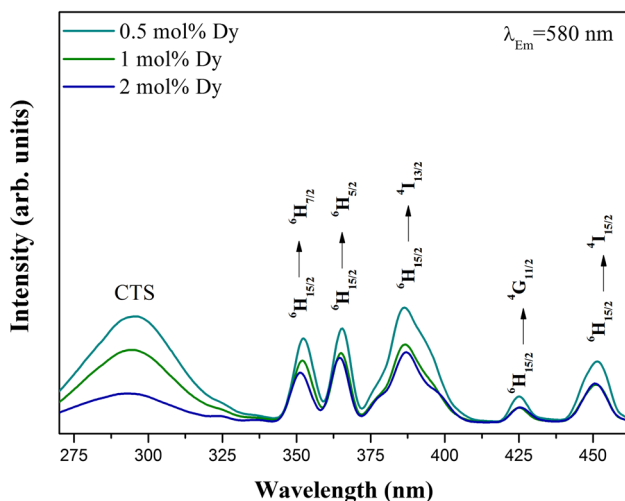


Fig. 8 PL excitation spectra of the $\text{ZnWO}_4:\text{Dy}^{3+}$ nanocrystals

which is assigned to the absorption of the WO_6^{6-} groups [52]. This indicates that energy transfer takes place from the distorted octahedral $[\text{WO}_6]$ clusters to Dy^{3+} ions in the $\text{ZnWO}_4:\text{Dy}^{3+}$ nanocrystals. This broad band corresponds to charge-transfer absorption from the $2p$ orbitals of the oxygen to the $5d$ orbitals of tungsten. The excitation spectra shows five other main absorption bands with peaks at 352, 365, 385, 424, and 452 nm and assigned to the ${}^6\text{H}_{15/2} \rightarrow {}^6\text{H}_{7/2}$, ${}^6\text{H}_{15/2} \rightarrow {}^6\text{H}_{5/2}$, ${}^6\text{H}_{15/2} \rightarrow {}^4\text{I}_{13/2}$, ${}^6\text{H}_{15/2} \rightarrow {}^4\text{G}_{11/2}$, and ${}^6\text{H}_{15/2} \rightarrow {}^4\text{I}_{15/2}$ transitions of Dy^{3+} ions, respectively [53].

Figure 9a–c illustrate the PL emission spectra at room temperature (excited at 298 nm), the energy level diagram, and the colorimetric data of $\text{ZnWO}_4:\text{Dy}^{3+}$ nanocrystals containing 0.5, 1, and 2 mol% of Dy^{3+} ions, respectively.

Tungstate materials themselves emit blue-green light under UV excitation. The excited tungstate groups can effectively transfer energy to doped lanthanide ions

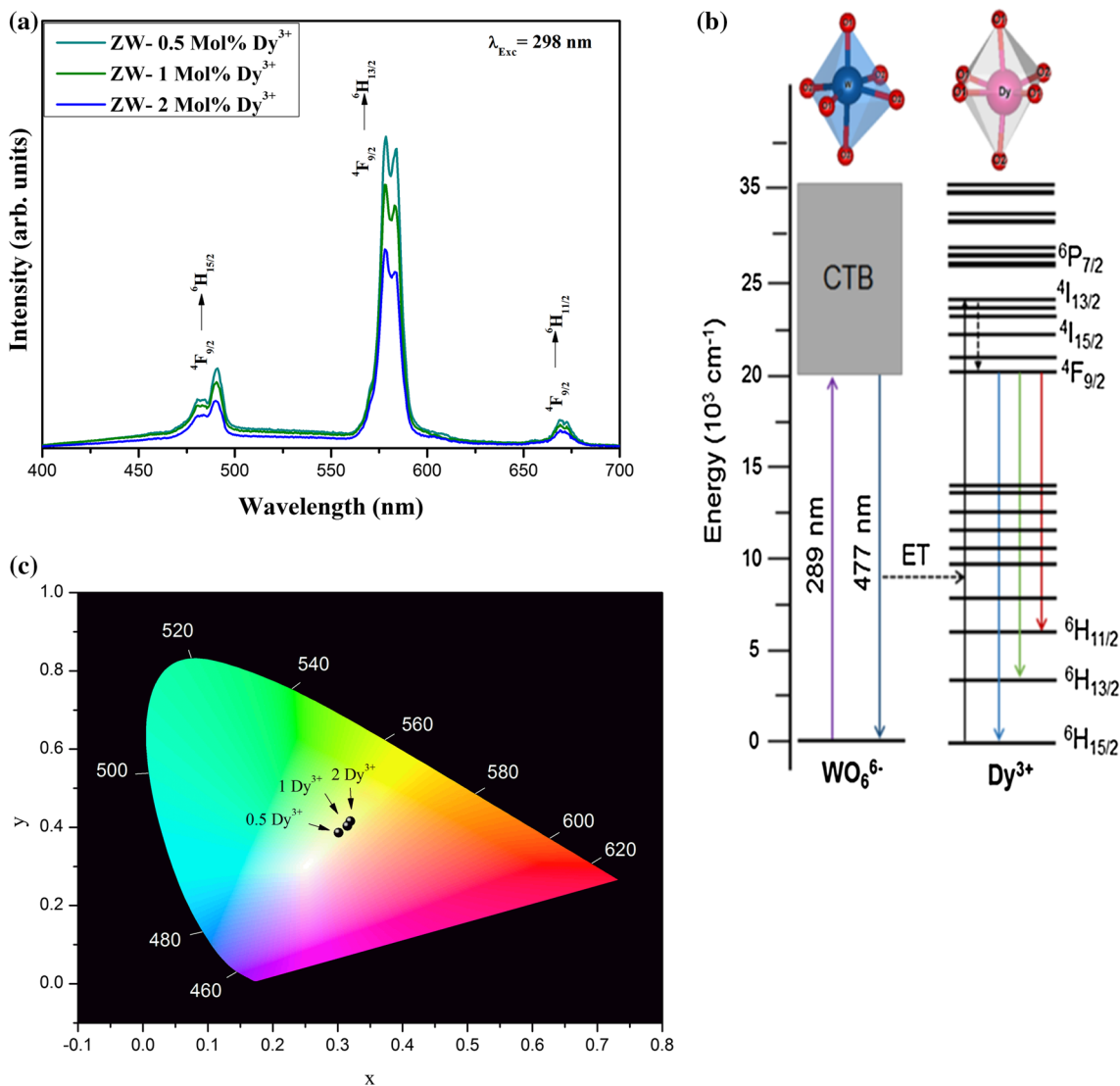


Fig. 9 a PL emission spectra at room temperature, **b** energy level diagram with proposed energy transfer mechanisms, and **c** colorimetric data of the ZnWO₄:Dy³⁺ nanocrystals

[54]. Pure ZnWO₄ crystals exhibit a broad PL emission band centered at approximately 477 nm [10], which is assigned to charge transfer transitions within the [WO₆] octahedral groups at levels very close to the energies of the VB and CB. This wide band corresponds to typical behavior for multiphonon or multilevel processes, which involve numerous energy states within the band gap [55]. Here, with the partial replacement of Zn²⁺ by Dy³⁺ ions, instead of this broad PL emission band, narrow lines ascribed to Dy³⁺ emissions are observed (Fig. 9a). For the Dy³⁺-doped ZnWO₄ samples, the observed spectral profile is related to the dopant concentration in the matrix. The peaks are ascribed to *f-f* transitions from the ground state to the excited states of the Dy³⁺ ions, which

indicate that efficient transfer of energy from the tungstate group to the lanthanide ions occurs.

As shown in Fig. 9a, upon excitation at 298 nm, the emission spectra of the ZnWO₄:Dy³⁺ nanocrystals shows the most intense emission lines in the range of 400–700 nm. The band at 580 nm corresponds to the hypersensitive ⁴F_{9/2} → ⁶H_{13/2} transition, which dominates the spectrum and is more intense than the other transitions. The bands at 480 and 489 nm can be ascribed to the ⁴F_{9/2} → ⁶H_{15/2} transition. The ⁴F_{9/2} → ⁶H_{11/2} transition was observed at 670 nm. All of the transitions associated with the observed emission lines are shown in the energy diagram in Fig. 9b. Upon excitation at 298 nm, the crystals are excited from the ground state to the excited state. Then, the matrix absorbs energy, resulting in light emission owing to charge transfer from the excited 2*p* orbitals of

Table 2 Chromatic coordinates x and y for $\text{ZnWO}_4:\text{Dy}^{3+}$ nanocrystals

[Dy ³⁺]/(mol%)	CIE coordinates	
	x	y
0.5	0.357	0.398
1	0.369	0.412
2	0.373	0.422

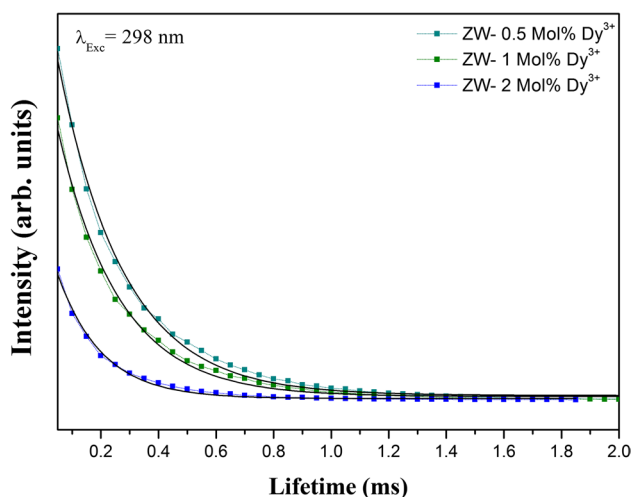
O^{2-} to the empty d orbitals of the central W^{6+} ions. In contrast, energy transfer from distorted octahedral $[\text{WO}_6]$ clusters to the ${}^4\text{I}_{13/2}$ state of Dy^{3+} ions is efficient.

Figure 9(c) shows the CIE (Commission International de l'Eclairage) coordinates of the $\text{ZnWO}_4:\text{Dy}^{3+}$ samples. Table 2 shows the corresponding chromatic coordinates x and y for the samples, which were determined to be [$x=0.357$, $y=0.398$], [$x=0.369$, $y=0.412$], and [$x=0.373$, $y=0.422$] for Dy^{3+} concentrations of 0.5, 1, and 2 mol%, respectively. These coordinates are close to those of standard white light ($x=0.333$, $y=0.333$). There are several approaches for generating white light sources using LEDs; among them, phosphor-based white light sources are the most promising [56].

The influence of the dopant ion concentration on the photoluminescent properties of these materials was investigated. Figure 10 depicts the PL decay curves of the ${}^4\text{F}_{9/2} \rightarrow {}^6\text{H}_{15/2}$ transition for Dy^{3+} in ZnWO_4 using emission and excitation at 580 and 298 nm, respectively. The decay curves are well fitted by second-order exponential decays, as shown in Eq. (13):

$$I(t) = I_0 + \alpha_1 e^{-t/\tau_1} + \alpha_2 e^{-t/\tau_2} \quad (13)$$

where I_0 and I are the luminescence intensities at times t and 0, respectively, α_1 and α_2 represent the pre-exponential factors (amplitude), and τ_1 and τ_2 are the corresponding

**Fig. 10** PL decay curves of the ${}^4\text{F}_{9/2} \rightarrow {}^6\text{H}_{15/2}$ transition for Dy^{3+} in ZnWO_4 nanocrystals. Black solid lines represent the fitting results

decay times. The average lifetime (τ), which is proportional to the total area under the fluorescence decay curve, is defined by Eq. (14):

$$\tau = (\alpha_1 \tau_1^2 + \alpha_2 \tau_2^2) / (\alpha_1 \tau_1 + \alpha_2 \tau_2) \quad (14)$$

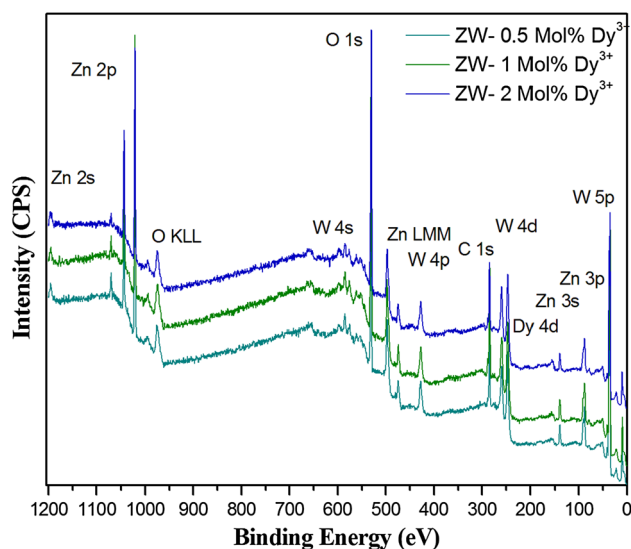
The data obtained by fitting the decay curves of the samples with different Dy^{3+} doping concentrations are listed in Table 3.

The average lifetimes of Dy^{3+} in the ZnWO_4 host lattices were calculated to be 0.28, 0.25, and 0.19 ms for dopant concentrations of 0.5, 1, and 2 mol% of Dy^{3+} , respectively. As can be seen, the 0.5 mol% Dy^{3+} -doped sample had the longest decay time (Fig. 10; Table 3). Moreover, this sample was found to have the strongest PL emission. Therefore, the optimal concentration of Dy^{3+} in ZnWO_4 is 0.5 mol%. With increasing lanthanide ion concentration, the decay time and the PL maxima intensity decreased because of concentration quenching from a non-radiative energy transfer between luminescence centers.

In this study, Dy^{3+} replaced Zn^{2+} ions in the ZnWO_4 network; therefore, charge compensation is required. Defects in the crystal lattice play a major role in determining the luminescent properties of the oxides [57], and by altering

Table 3 Lifetime, amplitude, and average lifetime of the PL decay curves for $\text{ZnWO}_4:\text{Dy}^{3+}$

T[Dy ³⁺]/(mol%)	Lifetime/(ms)			Amplitude	
	τ_1	τ_2	τ	α_1	α_2
0.5	0.11	0.33	0.28	77256	80522
1	0.29	0.09	0.25	71197	59978
2	0.23	0.07	0.19	31155	38635

**Fig. 11** XPS survey spectrum of the $\text{ZnWO}_4:\text{Dy}^{3+}$ samples

the content of some types of defects, the concentrations of the corresponding luminescence centers can be adjusted [58, 59]. In particular, vacancies are critical to the formation of luminescence centers in these crystals [60], and the vacancy content may be varied by appropriate doping of the

material. When the doped network is excited, the absorbed energy is lost by non-radiative energy transfer owing to ion–ion (Dy^{3+} – Dy^{3+}) interactions or by ion vacancies, i.e., defects generated by the insertion of the dopant into the host matrix, which sensitizes Dy^{3+} .

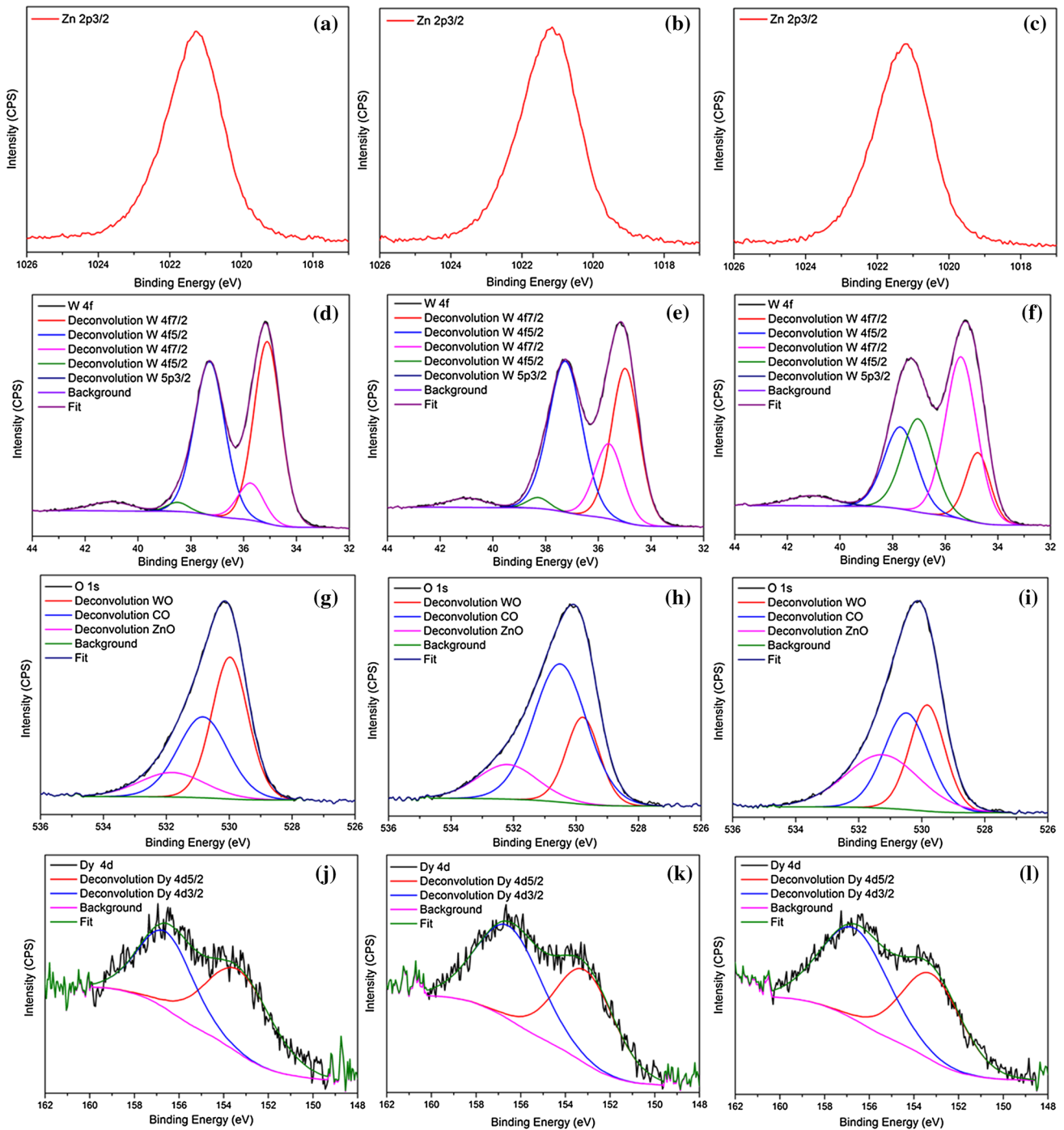


Fig. 12 Core level spectrum of **a, b** and **c** Zn $2p$ for the samples 0.5, 1 and 2 mol% of Dy^{3+} , respectively; **d, e** and **f** W $4f$ for the samples 0.5, 1 and 2 mol% of Dy^{3+} , respectively; **g, h** and **i** O $1s$ for the sam-

ples 0.5, 1 and 2 mol% of Dy^{3+} , respectively; **j, k** and **l** Dy $4d$ for the samples 0.5, 1 and 2 mol% of Dy^{3+} , respectively

However, we conclude that the interesting optical properties of $\text{ZnWO}_4:\text{Dy}^{3+}$ studied herein are dependent upon the particle size, given that the presence of the Dy^{3+} dopant reduced the size of the materials. It is well known that the luminescent properties of solids are strongly dependent on the particle size and morphology [58]. In general, the properties of nanostructures are different from those of the bulk due to the high surface area-to-volume ratio and possible appearance of quantum effects on the nanoscale. Duan and co-authors [62] studied the size-dependent optical properties of the nanoscale and bulk long-persistent phosphor $\text{SrAl}_2\text{O}_4:\text{Eu}^{3+}, \text{Dy}^{3+}$ prepared by auto-combustion of citrate gel. The change in the band gap of SrAl_2O_4 and the resulting change in the trap depth with particle size were discussed on the basis of analysis of the visible, excitation, and thermoluminescence (TL) spectra. The authors postulated that the emission-related energy levels of the Eu^{3+} activator and the persistent luminescence-related energy levels of the Dy^{3+} co-activator do not change very clearly with particle size. However, the band gap of the SrAl_2O_4 matrix crystal becomes wider with a decrease of the particle size because of the quantum effect. The smaller nanoparticles lead to more serious surface adsorption and surface defects, causing non-radiative relaxation and fluorescence quenching. They concluded that these factors are fatal for the long-persistent phosphors in nanoscale $\text{SrAl}_2\text{O}_4:\text{Eu}^{3+}, \text{Dy}^{3+}$. The afterglow of the nanoscale $\text{SrAl}_2\text{O}_4:\text{Eu}^{2+}, \text{Dy}^{3+}$ decays faster than that of the bulk counterpart.

X-ray photoelectron spectroscopy (XPS) was used to identify chemical composition, binding energy and oxidation state of components present on the material surface. The binding energies were obtained by calibrating the spectra through C 1s peak at 284.50 eV. Figure 11 shows the survey XPS spectrum of Dy doped ZnWO_4 samples. It was identified that the Zn 2p, W 4f, O 1s, and Dy 4d elements have existed in all of samples, confirming their compositions. The C 1s contamination peak can be ascribed to adventitious hydrocarbon from the XPS instrument.

The high resolution spectra of the main elements present in the samples are shown in Fig. 12. The high resolution Zn 2p spectrum in the range of 1026–1017 eV presents one peak at 1021 eV due to Zn 2p_{3/2} indicating the presence of Zn^{2+} ion. The high resolution W 4f spectra in the range of 44–32 eV present two components located at 37.3 and 35 eV which are due to the W 4f_{7/2} and W 4f_{5/2} respectively, and its confirm the W^{6+} oxidation state. Another two components at 38.3 and 35.6 eV can be ascribed to W^{5+} . The peak located at 41 eV is due to W 5p_{3/2}. The high resolution O 1s spectra in the range of 536–526 eV present one peak. Three components located at 529.8, 530.5 and 532.2 eV correspond to Zn–O bond, C–O, and W–O, respectively. There are some small variations in the intensity and area of these components because of the lower

atomic mass of oxygen. In addition, this element links the $[\text{WO}_6]$, $[\text{ZnO}_6]$ and $[\text{DyO}_6]$ clusters. The high resolution Dy 4d spectrum in the range of 162–148 eV presents one main peak at 156.6 eV. Two components located at 156.8 and 153.4 eV are due to Dy 4d_{3/2} and 4d_{5/2}, respectively. This result is similar to that of Dy 4d core level in Dy_2O_3 compound (156.0 eV) which is corresponding to the standard oxidation state of Dy^{3+} ions [63, 64].

4 Conclusions

In summary, we have successfully prepared $\text{ZnWO}_4:\text{Dy}^{3+}$ nanocrystals using a microwave-assisted hydrothermal method. For the first time, a systematic Rietveld refinement analysis provided insight into the structural properties of these materials. Furthermore, we have shown that, by varying the doping concentration of Dy^{3+} ions, the emission intensities and decay times can be easily tuned, and the crystalline $\text{ZnWO}_4:\text{Dy}^{3+}$ samples are single-material sources of white light. We hope this study will provide a new design rationale for luminescent materials for use in light display systems and optoelectronic devices with potential tunable white-light-emitting phosphors.

Acknowledgements The authors acknowledge financial support from the following Brazilian research funding institutions: FAPESP 2013/07296-2, 2013/07437-5, and 2013/23995-8; CNPq 304531/2013-8 and 307054/2015-2; and CAPES/PROCAD 182441.

References

1. K. Feng, S. Huang, Z. Lou, N. Zhu, H. Yuan, Dalton Trans **44**, 13681–13687 (2015)
2. W. Li, L. Cao, X. Kong, J. Huang, C. Yao, J. Fei, J. Li, RSC Adv **6**, 23783–23789 (2016)
3. S.C. Sabharwal, Sangeeta, J. Cryst. Growth **200**, 191–198 (1999)
4. S. Ran, L. Gao, Chem. Lett. **35**, 1312–1313 (2006)
5. T. Oi, K. Takagi, T. Fukazawa, Appl. Phys. Lett. **36**, 278–279 (1980)
6. D. Li, J. Xue, X. Bai, CrystEngComm **18**, 309–315 (2016)
7. K. Wang, W. Feng, X. Feng, Y. Li, P. Mi, S. Shi, Spectrochim. Acta A **154**, 72–75 (2016)
8. C. Li, X. Du, D. Yue, J. Gao, Z. Wang, Mater. Lett. **108**, 257–260 (2013)
9. V. Bedekar, D.P. Dutta, M. Mohapatra, S.V. Godbole, R. Ghildiyal, A.K. Tyagi, Nanotechnology **20**, 125707–125715 (2009)
10. Y.X. Zhou, L. Tong, X.B. Chen, X.H. Zeng, Appl. Phys. A **117**, 673–679 (2014)
11. C.S. Lim, J. Ceram. Process. Res. **12**, 140–145 (2011)
12. J.C. Yu, C. Yu, Mater. Sci. Eng. B **164**, 16–22 (2009)
13. X. Sun, X. Li, X. Dan Sun, J. He, B. Wang, J. Mater. Sci. **25**, 1647–1651 (2014)
14. R. Shi, Y. Wang, D. Li, J. Xu, Y. Zhu, Appl. Catal. B **100**, 173–178 (2010)
15. I.M. Pinatti, I.C. Nogueira, W.S. Pereira, P.F.S. Pereira, R.F. Gonçalves, J.A. Varela, E. Longo, I.L.V. Rosa, Dalton Trans **44**, 17673–17685 (2015)

16. Y. Tang, S. Yang, Q. Zhu, X. Liao, *Mod. Res. Catal.* **5**, 45–49 (2016)
17. L. Pan, X. Liu, Z. Suna, C.Q. Sun, *J. Mater. Chem. A* **1**, 8299–8326 (2013)
18. G. Blasse, H.C.G. Verhaar, M.J.J. Lammers, G. Wingefeld, R. Hoppe, P. De Maayer, *J. Lumin.* **29**, 497–499 (1984)
19. R.C. Dai, Z.P. Wang, Z.M. Zhang, Z.J. Ding, *Surf. Interface Anal.* **46**, 1151–1155 (2014)
20. R. Shrivastava, J. Kaur, V. Dubey, *J. Fluoresc.* **26**, 105–111 (2016)
21. N. Shinde, N.S. Dhoble, S.C. Gedam, S.J. Dhoble, *J. Lumin.* **172**, 131–138 (2016)
22. D.V. Sunitha, H. Nagabhushana, S.C. Sharma, B.M. Nagabhushana, P.B. Daruka, R.P.S. Chakradhar, *Spectrochim. Acta A* **127**, 381–387 (2014)
23. J. Wang, J. Wang, P. Duan, *Mater. Lett.* **107**, 96–98 (2013)
24. K. Pavani, J.S. Kumar, T. Sasikala, B.C. Jamalaiah, H.J. Seo, L.R. Moorthy, *Mater. Chem. Phys.* **129**, 292–295 (2011)
25. R. Shrivastava, J. Kaur, M. Dash, *Superlattices Microstruct.* **82**, 262–268 (2015)
26. Y. Ji, J. Cao, Z. Zhu, J. Li, Y. Wang, C. Tu, *J. Lumin.* **132**, 702–706 (2012)
27. Y. Zhai, M. Wang, Q. Zhao, X. Li, J. Yu, *J. Lumin.* **172**, 161–167 (2016)
28. A.N. Yerpude, S.J. Dhoble, B. Ramesh, B.D.P. Raju, *Adv. Mater. Lett.* **6**, 1111–1115 (2015)
29. J. Kuang, Y. Liu, J. Zhang, *J. Solid State Chem.* **179**, 266–269 (2006)
30. N.V. Minh, N.M. Hung, D.T.X. Thao, M. Roefiaers, J. Hofkens, *J. Spectrosc.* **2013**, 1–5 (2013)
31. Y. Zhai, M. Wang, Q. Zhao, H. Yang, H. Ding, *J. Mater. Sci.* **27**, 279–285 (2016)
32. K. V. Dabre, S. J. Dhoble, *Recent Res. Sci. Technol.* **4**, 102–103 (2012)
33. A. Phuruangrat, P. Dumrongrojthanath, S. Thongtem, T. Thongtem, *Mater. Lett.* **166**, 183–187 (2016)
34. A.C. Larson, R.B. Von Dreele, *General Structure Analysis System (GSAS)*. (Los Alamos National Laboratory, Los Alamos, 1994)
35. H.M. Rietveld, *J. Appl. Cryst.* **2**, 65–71 (1969)
36. P. Thompson, D.E. Cox, J.B. Hastings, *J. Appl. Cryst.* **20**, 79–83 (1987)
37. L.W. Finger, D.E. Cox, A.P.A. Jephcoat, *J. Appl. Cryst.* **27**, 892–900 (1994)
38. P.W. Stephens, *J. Appl. Cryst.* **32**, 281–289 (1999)
39. P.F. Schofield, K.S. Knight, S.A.T. Redfern, G. Cressey, *Acta Crystallogr. Sect. B* **53**, 102–112 (1997)
40. K. Momma, F. Izumi, *J. Appl. Crystallogr.* **44**, 1272–1276 (2011)
41. A. Kalinko, A. Kuzmin, *J. Non-Cryst. Solids* **357**, 2595–2599 (2011)
42. G. He, H. Fan, L. Ma, K. Wang, D. Ding, C. Liu, Z. Wang, *Mater. Sci. Semicond. Process.* **41**, 404–410 (2016)
43. S.R. Ede, A. Ramados, U. Nithiyanantham, S. Anantharaj, S. Kundu, *Inorg. Chem.* **54**, 3851–3863 (2015)
44. M. Banyay, M. Sarkar, A. Graslund, *Biophys. Chem.* **104**, 477–488 (2003)
45. A.G.M. Silva, T.S. Rodrigues, A. Dias, H.V. Fajardo, R.F. Gonçalves, M. Godinho, P.A. Robles-Dutenhefner, *Catal. Sci. Technol.* **4**, 814–821 (2014)
46. R.F. Gonçalves, M.J. Godinho, A.P.A. Marques, M.R.C. Santos, I.L.V. Rosa, E. Longo, M. Siu Li, J.L.S. Sa, L.S. Cavalcante, *Electron. Mater. Lett.* **11**, 193–197 (2015)
47. P. Kubelka, F. Munk-Aussig, *Zeit. Für, Tech. Physik.* **12**, 593–601(1931)
48. I.L. Validzic, T.D. Savic, R.M. Krsmanovic, D.J. Jovanovic, M.M. Novakovic, M.C. Popovic, M.I. Comor, *Mater. Sci. Eng. B* **177**, 645–651 (2012)
49. L.S. Cavalcante, V.M. Longo, J.C. Sczancoski, M.A.P. Almeida, A.A. Batista, J.A. Varela, M.O. Orlandi, E. Longo, M. Siu Li, *CrystEngComm* **14**, 853–868 (2012)
50. F.Y. Lo, Y. Ting, K. Chou, T. C. Hsieh, C. Ye, Y. Hsu, M. Chern, H. Liu, *J. Appl. Phys.* **117**, 213911–213915 (2015)
51. A.V. Prokofiev, A.I. Shelykh, B.T. Melekh, *J. Alloys Compd.* **242**, 41–47 (1996)
52. X. Sun, X. Sun, X. Li, J. He, B. Wan, *J. Electron. Mater.* **43**, 3534–3538 (2014)
53. X. Liu, W. Xiang, F. Chen, Z. Hu, W. Zhang, *Mater. Res. Bull.* **48**, 281–285 (2013)
54. A.M. Kaczmarek, K. Van Hecke, R. Van Deun, *Inorg. Chem.* **53**, 9498–9508 (2014)
55. R.F. Gonçalves, L.S. Cavalcante, I.C. Nogueira, E. Longo, M.J. Godinho, J.C. Sczancoski, V.R. Mastelaro, I.M. Pinatti, I.L.V. Rosa, A.P.A. Marques, *CrystEngComm* **17**, 1654–1666 (2015)
56. P. Nimishe, S. J. Dhoble, *Bull. Mater. Sci.* **34**, 1119–1125 (2011)
57. S. Shi, X. Liu, J. Gao, J. Zhou, *Spectrochim. Acta Part A* **69**, 396–399 (2008)
58. M. Jiang, X.D. Xue, Z.Q. Chen, Y.D. Liu, H.W. Liang, H.J. Zhang, A. Kawasuso, *J. Mater. Sci.* **49**, 1994–1999 (2014)
59. Q. Zhang, H. Sun, X. Wang, Y. Zhang, X. Li, *J. Eur. Ceram. Soc* **34**, 1439–1444 (2014)
60. O. Chukova, S. Nedilko, V. Scherbatskyi, *Opt. Mater.* **34**, 2071–2075 (2012)
61. Y. Yang, X. Li, W. Feng, W. Yang, W. Li, C. Tao, *J. Alloys Compd.* **509**, 845–848 (2011)
62. X. Duan, L. Yi, X. Zhang, S. Huang, *J. Nanomater.* **2015**, 1–7 (2015)
63. J.S. Mohamed, M.K. Bhat, *AIMS Mater. Sci.*, **4**, 158–171 (2017)
64. R. Tholkappian, K. Vishista, *Appl. Surf. Sci.* **251**, 1016–1024 (2015)